Direct observation of pore collapse and tensile stress generation on pore walls due to salt crystallization in a PDMS channel

Antoine Naillon, Pierre Joseph, Marc Prat

Direct observation of pore collapse and tensile stress generation on pore walls due to salt crystallization in a PDMS channel

Antoine Naillon, [abc] Pierre Joseph[b] and Marc Prat*[a]

The generation of stress on pore walls due to salt crystallization is generally analysed as a compressive stress generation mechanism using the concept of crystallization pressure. We report on a completely different stress generation mechanism. In contrast with the classical picture where the crystal pushes the pore wall, the crystal growth leads to the generation of a local tensile stress. This tensile stress occurs next to a region where a compressive stress is generated, thus inducing also shear stresses. These findings are obtained from direct optical observations in PDMS model pores where the tensile stress generation results in the collapse of the pore region located between the crystal and the pore dead-end. The experiments also reveal other interesting phenomena, such as hyperslow drying in PDMS channels or asymmetrical growth of the crystal during the collapse.

During evaporation from a porous medium containing dissolved salts, the salt concentration increases and can reach a sufficient concentration for salt crystals to form. As reported for example in ref. 1–3, the presence of the ions can dramatically change the drying kinetics owing to the formation of a salt crust or pore clogging. Still more importantly in relation to civil engineering and cultural heritage conservation issues,[4] crystal formation can cause severe damage and cracks in porous materials,[5–7] sometimes leading to complete destruction.[8] The stress generation mechanism leading to damage is generally associated with the concept of crystallization pressure, see ref. 9–11 and references therein. The latter can be expressed for sufficiently large crystals of sodium chloride (>1 μm) as (only NaCl is considered throughout this paper),

$$P_c = \frac{2RT}{V_m}\left(\ln S + \ln\frac{\gamma_\pm}{\gamma_{\pm,0}}\right) \quad (1)$$

where R is the ideal gas constant, T is the temperature, V_m is the molar volume of the solid phase forming the crystal (V_m = 27.02 cm^3 mol^{-1} for NaCl), and $\gamma_\pm$ is the ion mean activity coefficient. Index 0 refers to the reference state where the crystal is in equilibrium with the solution in the absence of stress applied on the crystal. The ratio $S = m/m_0$ is the supersaturation, where m denotes the molality of the solution ($S = 1$ when the crystal and the solution are in equilibrium in the reference state). According to eqn (1), stress can be generated when the solution in contact with the crystal is supersaturated ($S > 1$). Although supersaturation as high as 1.7 has been measured,[12–14] the stress actually generated cannot be readily deduced from eqn (1). As discussed in ref. 11, what matters is not the supersaturation at the crystallization onset but the supersaturation when the crystal is about to clog the pore, *i.e.* when the crystal is separated from the wall only by a very thin liquid film in which a disjoining pressure can develop.[10] The latter is generally much smaller owing to the local consumption of ions near the growing crystal during its growth. The net result, however, when the conditions are met for the supersaturation to be sufficiently high in the thin liquid film, is the generation of a normal compressive stress on the pore wall, meaning here that the crystal tends to "push" the wall.[11]

In what follows we observe a completely different mechanism of stress generation, leading, at least for our system, to stresses comparable in magnitude with the stresses due to crystallization pressure. In contrast with the classical case, however, the generated normal stress is not compressive but tensile and this results in the collapse of the dead-end section of the pore.

The study is based on observations in a microfluidic device where the crystallization is generated by evaporation of a NaCl aqueous solution confined in dead-end channels. In addition to the pore collapse, the experiments reveal interesting phenomena such as hyperslow evaporation kinetics, crystallization induced acceleration of the receding meniscus and the preferential

[a] *Institut de Mécanique des Fluides de Toulouse (IMFT), Université de Toulouse, CNRS, Toulouse, France. E-mail: mprat@imft.fr; Tel: +33 (0)5 34 32 28 83*

[b] *LAAS-CNRS, Université de Toulouse, CNRS, Toulouse, France*

[c] *Univ. Grenoble Alpes, CNRS, Grenoble INP, LRP, 38000 Grenoble, France*

† Electronic supplementary information (ESI) available. See DOI: 10.1039/c8sm02546k

growth of a crystal on the side of the dead-end section of the channel, thus shedding light on the rich physics of crystal growth at the pore scale.

2 Experimental

The microfluidic device and its fabrication procedure have been presented in previous papers[11,14] and therefore are only briefly described here (see however ESI† Appendix A for a figure and additional details). Evaporation experiments of a saline aqueous solution are performed in dead-end square channels of a $4.5 \times 4.5\ \mu m^2$ cross section surface area, referred to as pore channels. The channel length is 200 μm. The chips containing the channels are of PDMS and glass. The glass is used for the cover plate closing the PDMS channels. The salt solution is prepared with NaCl provided by Sigma Aldrich© dissolved in deionized water. Unless otherwise mentioned, the initial molality of the solution is 1.89, the saturation in the reference state being 6.15 mol kg^{-1} (corresponding to mass fractions of 10% and 26.4% respectively). The salt purity is ensured to be higher than 99.5%.

Experiments are performed using an inverted microscope Zeiss Axio observer D1 working in transmission mode. The dead-end channels are filled with a salt solution of known concentration. Then, they are dried maintaining a nitrogen flow at their entrances during all of the experiment.

Crystallization starts once a critical salt concentration is reached in the pore channel. An Andor Zyla SCMos camera is used to record the kinetics of evaporation with a frame rate of 2 seconds per image.

3 Results and discussion

3.1 Observations

A meniscus forms and progressively recedes into each pore channel. During the evaporation of the salt solution, only water evaporates whereas the dissolved species remain trapped in the solution. As a result, the salt concentration increases to reach a higher value than the equilibrium one. This meta-stable state lasts until the onset of crystallization. Once nucleation occurs, a crystal grows consuming the ions in excess above the equilibrium concentration. At the same time, the solution continues to evaporate providing more salt for crystal growth. This sequence is illustrated in Fig. 1.

As can be seen, the formation of the crystal first leads to the compression of the PDMS around the crystal, which in Fig. 1 results in a larger width of the channel in the crystal zone. This is better illustrated in Fig. 2a, which shows the variation of the crystal width as a function of time. For more details on the compressive stress generation, one can refer to ref. 11 where a stress diagram summarizing the conditions leading to the stress generation is presented. Fig. 1 also shows an unexpected phenomenon: the collapse of the channel on the dead-end side, *i.e.* the section of the channel located between the most advanced face of the crystal and the channel dead-end. As can be seen, the collapse is progressive and the crystal continues to grow during the collapse period. However, as better shown in Fig. 2, the crystal growth takes place only on the right, *i.e.* where the crystal is in contact with the collapsing region. Note that the back face is defined as the crystal face on the side of the pore channel open end whereas the front face is the face of the crystal on the side of the pore channel dead-end, thus the most advanced face into the channel. The width of the collapsing region is the minimum width in the images of the collapsing region. It roughly corresponds to the width in the middle of the collapsing region.

3.2 Hyperslow drying

In addition to this unexpected collapse phenomenon, the experiments reveal several other interesting phenomena. First, as illustrated in Fig. 3, the receding meniscus kinetics is much slower than expected if one assumes that the evaporation should follow the classical Stefan's tube evaporation kinetics.[15] The latter predicts that the receding meniscus position in the tube (the distance between the channel open end and the meniscus) varies as $\sqrt{2D_v\rho_{vs}t/\rho_\ell}$ where t is the time, D_v is the molecular diffusion of the water vapor in nitrogen, ρ_ℓ is the solution density, and ρ_{vs} is the water vapor concentration at the meniscus surface. To obtain the result shown in Fig. 3, we have taken for simplicity the value of ρ_{vs} corresponding to a sodium chloride saturated solution. Note that the experimental results shown in Fig. 3 are for an initial salt fraction of 20% (and not 10% as for the other results shown in the papers). This is just because the data of the meniscus position are available right from the beginning for this particular experiment.

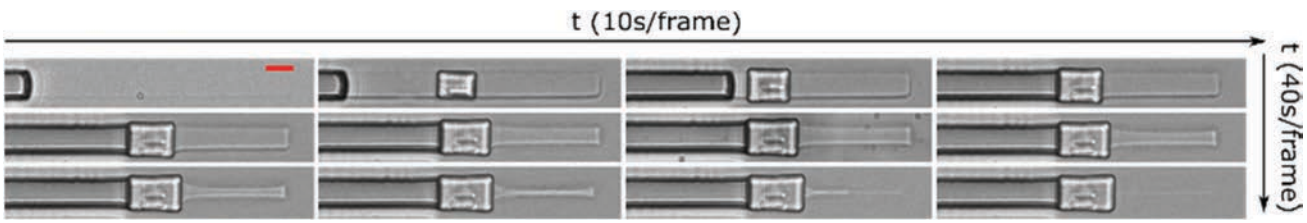

Fig. 1 Channel deformation resulting from the growth of a single cluster. A crystal appears in a channel of a $4.5 \times 4.5\ \mu m^2$ cross-section surface area at some distance from the receding meniscus (visible on the left in the first three top images) and clogs it. The crystal growth first induces a positive deformation when the crystal touches the wall and continues to grow. The meniscus continues receding. When it reaches the crystal, the channel wall on the right of the crystal starts to collapse. At the end, the channel on the right of the crystal is totally closed. The red scale bar represents 5 μm.

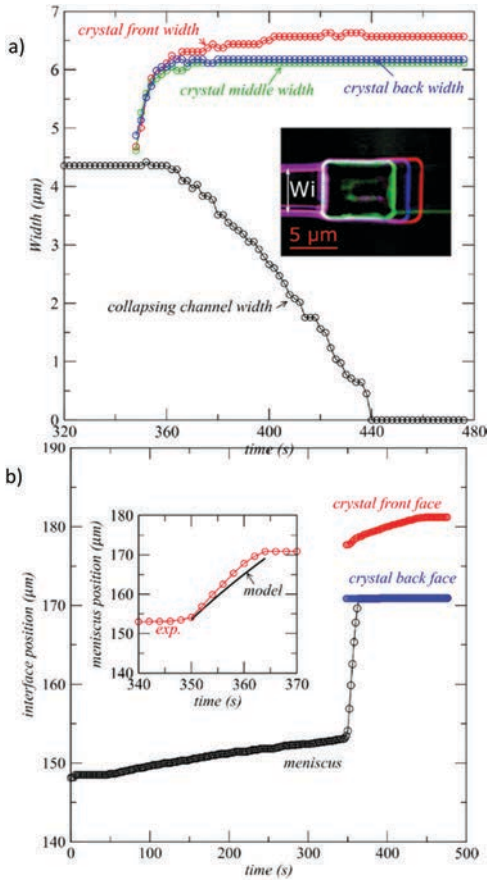

Fig. 2 (a) Variation of the channel width in the collapsing region and the crystal back and front face widths as a function of time. The inset shows superimposed images of the crystal contour at three different times. Growth occurs on the right side of the crystal, *i.e.* on the side of the channel collapsing region; W_i is the initial channel width. (b) Variation of the meniscus, crystal back face and crystal front face positions as a function of time. The position is the distance from the pore channel open end. The inset shows the comparison between model (see ESI† Appendix C) and experimental results in the acceleration period of the meniscus.

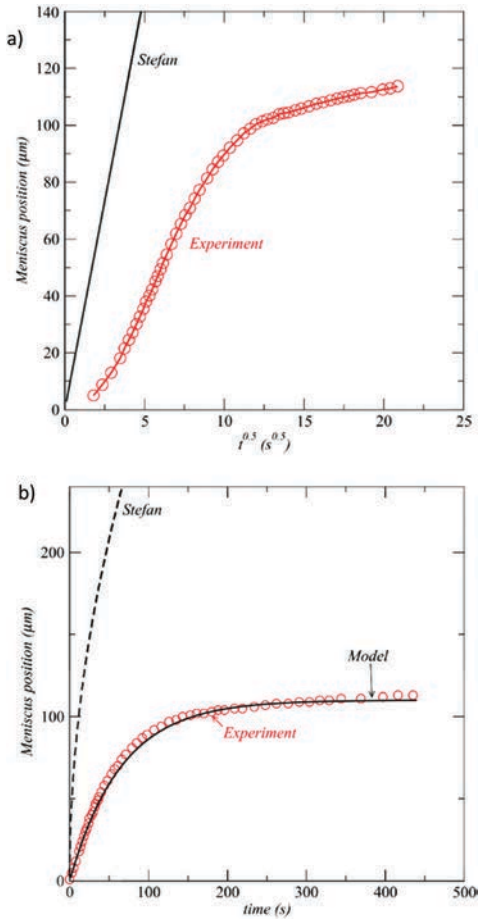

Fig. 3 Hyperslow evaporation kinetics in the channel. (a) Meniscus position as a function of the square root of time. The curve labelled "Stefan" corresponds to the classical diffusion controlled evaporation kinetics in a straight tube. (b) Comparison between the experiment and the pervaporation–condensation model described in ESI† Appendix B.

The experiments have been performed several times with different configurations (geometry and initial concentration) and hyperslow drying has always been observed.

To explain the hyperslow evaporation depicted in Fig. 3, it should be recalled that water can actually migrate into PDMS.[16–20] Since the chip is first invaded by the solution for several minutes before the evaporation starts, the PDMS is actually saturated with water, at least near the pore channel and supply channel walls. The simple model taking into account the pervaporation process presented in ESI† Appendix B leads to the comparison with the experimental data shown in Fig. 3. As illustrated in Fig. 3, it leads to consistent results with the experiment. However, one might wonder why the meniscus motion is (much) slower than predicted by Stefan's model. One might think that the pervaporation process acts in addition to the vapor diffusion transport within the channel. Accordingly, the meniscus motion should be faster than predicted by Stefan's model. The explanation is the following. Due to the presence of water in the channel PDMS walls, water is actually transferred from the wall into the gas phase in the channel (see a schematic of the process in ESI† Appendix B). Thus, the vapor concentration in the gas in the channel is expected to be close to the saturation vapor concentration, $\rho_v \sim \rho_{vs}$. As a result, the vapor concentration gradient along the channel is much less than in the classical Stefan's situation. In other words, the vapor diffusive transport in the channel is expected to be negligible. In summary: (i) the pervaporation process and the humidity inside the PDMS are responsible for the very slow meniscus motion in the channel, and (ii) the meniscus motion is very slow at the onset of crystallization (which occurs right at the end of the period shown in Fig. 3b).

3.3 Meniscus sudden acceleration

As shown in Fig. 2b, the meniscus suddenly and strongly accelerates when $t \approx 350$ s. As can be seen from Fig. 2b, this strong acceleration (the change in the slope of the meniscus position curve in Fig. 2b is by a factor of about 70) is concomitant with the crystal growth in the channel. This acceleration is explained by two phenomena. The less important one is related to the deformation of the channel induced by the crystal growth near the crystal back face. A simple volume conservation argument

implies the acceleration of the meniscus because of the channel cross section surface area increase due to the channel deformation by the crystal. According to the model presented in ESI† Appendix C, the second phenomenon is more important. Owing to the greater density of the crystal compared to the salt concentration in the solution, the growth of the crystal induces a liquid flow in the direction of the growing crystal interface.[11] This flow induces in turn the acceleration of the meniscus. As depicted in the inset in Fig. 2b, a simple model taking into account both phenomena (see ESI† Appendix C) leads to good agreement with the experimental data.

3.4 Crystal front face longitudinal growth

To explain now the growth of the crystal at the front and not at the back depicted in Fig. 2, we first note that the back face transverse growth stops when the meniscus reaches the crystal (compare Fig. 2a and b). This indicates that this growth should correspond to the precipitation of the ions contained in the liquid plug on the left of the crystal, *i.e.* the liquid plug between the crystal back face and the receding meniscus. The fact that this growth stops when this liquid plug disappears is an indication that few ions, if any, are transported from the channel collapsing region up to the crystal back face. This is also consistent with the fact that the evaporation at the meniscus is too weak to induce a noticeable liquid flow in the direction of the channel entrance during the time of crystal growth. The noticeable growth of the front face is analyzed similarly. This growth must correspond to the precipitation of the ions contained in the channel collapsing region. Assuming that the salt concentration in the collapsing region is the equilibrium concentration (which is consistent with the results reported in ref. 13 and 14 showing that the ions in excess at the crystallization onset are very rapidly consumed), a simple mass conservation model based on this assumption (see ESI† Appendix D) leads to the comparison depicted in Fig. 4. The favorable comparison between this model and the experiment supports the proposed analysis.

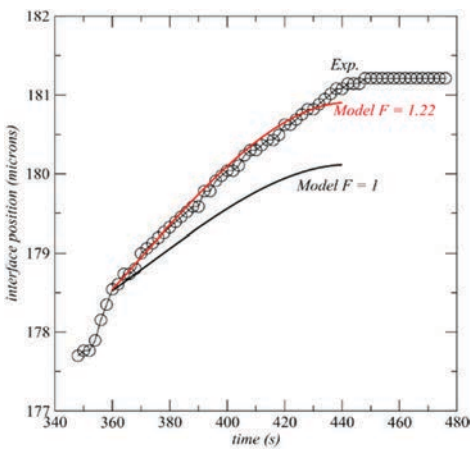

Fig. 4 Crystal front face position as a function of time. Comparison between the experimental data and a model based on the assumption that the crystal front face growth is due to the precipitation of ions contained in the collapsing liquid plug. Parameter F is a shape factor characterizing the shape of the collapsing region cross section surface area (see ESI† Appendix D).

3.5 Crystal front face transverse growth

Then, we have to explain why only the advancing region of the crystal grows transversally and pushes the wall and not the region of the crystal located further away from the advancing crystal face. We first note that the disappearance of the liquid in the collapsing region cannot be explained by the evaporation in the region of the crystal back face since the evaporation is, as discussed previously, quite low at the receding meniscus just before the crystal grows and the collapse occurs. Noting that the halite (the crystallized form of sodium chloride) is anhydrous, the conclusion is that water leaves the collapsing region through pervaporation of water through the PDMS, *e.g.* ref. 16–20. Thus, as schematically illustrated in Fig. 5, the picture is that water leaves the collapsing region by pervaporation through the PDMS while ions precipitate on the crystal. Thus, the collapse kinetics is controlled by the pervaporation process. The pervaporation velocity v_{pe} is estimated in ESI† Appendix E as being $v_{pe} = 2.3 \times 10^{-8}$ m s^{-1}.

Also, we consider the somewhat classical picture[5,10,21,22] where a thin liquid film of thickness h is present between the crystal and the channel wall. This film is necessary for the transverse growth of the crystal since ions must access the crystal surface to make it grow. The film is sketched in Fig. 5. Then the model of the ion transport in the film presented in ESI† Appendix F leads to the height-averaged ion mass fraction profiles depicted in Fig. 6. According to the classical diffusion reaction theory (DRT),[23] the crystal growth is analyzed as a reaction process during which ions fit in the crystal lattice. The latter is expressed as

$$w_{cr} = \frac{k_r \rho_\ell}{\rho_{cr}}(C_i - C_{eq}) \qquad (2)$$

where w_{cr} (m s^{-1}) is the local crystal growth rate; k_r (m s^{-1}) is the reaction (precipitation) coefficient, C_i (unitless) is the ion mass fraction at the crystal surface, C_{eq} is the ion mass fraction at equilibrium and ρ_{cr} is the crystal density (kg m^{-3}). Thus the ion mass fraction in the solution must be (slightly) greater than C_{eq} for the crystal to grow. The profiles depicted in Fig. 6 are thus fully consistent with the experiments since they indicate that the growth occurs only in the region of the film located in the very close vicinity of the front face of the crystal.

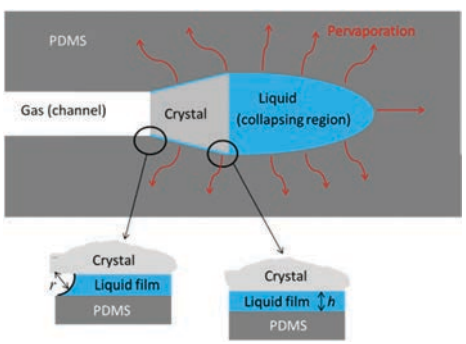

Fig. 5 Schematic of the channel collapse situation assuming a thin film between the crystal and the wall with a meniscus stuck at the tip of the liquid film on the back side of the crystal during collapse. The red arrows represent the pervaporation process.

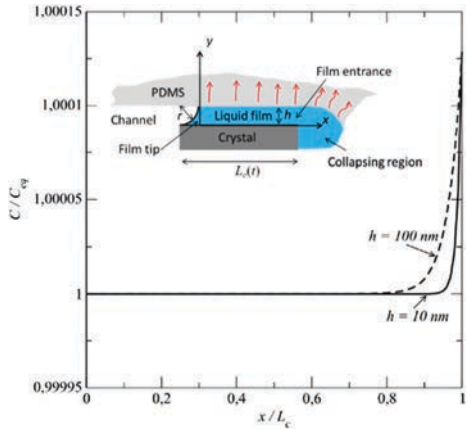

Fig. 6 Ion mass fraction distribution along the film for two thicknesses of the film. The inset shows a schematic of the thin film between the crystal and the wall with notations. For the sake of clarity, the ratio h/L_c in the inset is not to scale ($h \sim$ 10–100 nm, $L_c \sim$ 10 μm).

Further away from the film entrance $C \sim C_{eq}$, which is consistent with the observation of no transverse growth away from the crystal front face (Fig. 2a). Since the experimental observation indicates that the transverse growth is quite localized at the edge of the crystal front face the results plotted in Fig. 6 suggest that the film thickness is closer to 10 nm than 100 nm. This is consistent with the thicknesses reported in ref. 22 where another interesting situation where transport phenomena in the film control the growth of a confined crystal is analyzed. As explained in ESI† Appendix F the ion mass fraction C_{L_c} at the entrance of the film ($x = L_c(t)$) is estimated from the measured growth rate of the crystal and eqn (2). This yields $C_{L_c}/C_{eq} = 1.00013$.

Although the consideration of a liquid film between the crystal and the wall all along the crystal leads to consistent results with the observation, we have no direct experimental proof of the existence of this film. What is needed and clear from Fig. 6 is that the liquid film must exist at least in the region where the crystal grows, *i.e.* in the region of the front face of the crystal. So perhaps, there is no film away from this region (as the result of the pervaporation). Accordingly, the PDMS would be in contact with the walls where there is no lateral growth and the liquid film trapped between the crystal and the wall only on the crystal front face side.

3.6 Mechanical considerations

Another reasonably consistent aspect lies in the value of the crystallization pressure corresponding to the estimate of the ions in excess at the film entrance depicted in Fig. 6 ($C_{L_c}/C_{eq} = 1.00013$). To this end, we consider the mechanical equilibrium in the film region. Assuming negligible wall and crystal curvature effects, this (quasi-static) mechanical equilibrium can be expressed as[21]

$$\sigma = -p_s - p_d \quad (3)$$

where σ is the normal stress on the pore wall (negative when compressing the wall using the same convention as in ref. 21), p_s is the pressure in the solution and p_d is the disjoining pressure.[24] According to the analysis presented in ref. 21, $p_d \sim P_c$, where P_c is the crystallization pressure (eqn (1)). Note that only equilibrium situations are considered in the analysis presented in ref. 21. We thus assume that this analysis is still acceptable under non-equilibrium conditions, *i.e.* during the crystal growth. The pressure p_s in the solution is expressed as $p_{atm} - P_{cap}$, where p_{atm} is the atmospheric pressure (pressure in the gas phase) and P_{cap} is the capillary pressure (the pressure jump between the liquid and gas phase through the meniscus sketched in Fig. 5). Introducing a capillary pressure is consistent with the assumption of the liquid film as sketched in Fig. 5. However, as discussed later, the presence of a meniscus can be questioned. In this case, P_{cap} can be seen as just a way of parametrizing the variation of p_s, *i.e.* the fact that the pressure in the solution must decrease during the collapse. Thus, eqn (3) is finally expressed as,

$$\sigma + p_{atm} = P_{cap} - P_c \quad (4)$$

The computations reported in ref. 11 indicate that the compressive stress necessary to observe a channel deformation of 5 μm is about −0.5 MPa. In the present experiment (Fig. 2a), the channel deformation is less: ∼1.3 μm, based on the variation of the crystal back width in Fig. 2a. As a result, the compressive stress σ_{eq} to observe this deformation is expected to be on the order of $-0.5 \times 1.3/5 \sim 0.13$ MPa. As computed in ESI† Appendix G, it is expected that the capillary pressure is on the order of 0.5 MPa at most. Thus P_{cap} varies between approximately zero (beginning of the collapse) and 0.5 MPa (end of the collapse) during the collapse. From eqn (4), we can then deduce the variation of P_c during the collapse, *i.e.* between t = 360 s and 440 s (see Fig. 2a). Then using eqn (1), we can determine the variation of C_{eq}/C_{sat} during the collapse (C_{eq} is the ion mass fraction in the film away from the crystal front face, where no additional crystal growth occurs, see ref. 13 for the relation between the ion mass fraction and molality; C_{sat} is the solubility, *i.e.* the equilibrium ion mass fraction in the solution in the absence of stress applied on the crystal, *i.e.* in the reference state). The values so obtained are reported in Table 1. In the region of the film adjacent to the crystal front face where the transverse deformation occurs, the compressive stress, and thus the crystallization pressure, must be greater so as to cause the additional transverse deformation. Assuming an elastic deformation, the compressive stress causing the additional transverse deformation is proportional to the additional displacement, hence $\sigma(L_c(t)) = \sigma_{eq} e(L_c(t))/e_{eq}$ where, as depicted in Fig. 6, L_c is the length of the crystal. The displacement e is defined as $e = W - W_i$ where W_i is the initial width of the channel and W is the width of the channel after deformation. With $e(L_c(t)) \sim$ 1.69 μm and $e_{eq} \sim$ 1.3 μm (from the data shown in Fig. 2a), this gives $\sigma(L_c(t)) \sim -0.17$ MPa. This corresponds to the maximum deformation which is observed between t = 400 s and t = 440 s in Fig. 2a. A simple consideration is to assume that $\sigma(L_c(t))$ varies linearly between −0.13 MPa and −0.17 MPa with t for t varying between 360 s and 400 s, *i.e.* in the period before the maximum deformation is reached. Using again eqn (4) (with $\sigma = \sigma(L_c(t))$)

Table 1 Variation of $C(L_c(t))/C_{eq}$ as a function of time during the collapse. The capillary pressure P_{cap} and the compressive normal stress σ are in MPa

t (s)	P_{cap}	$\sigma(L_c(t))$	C_{eq}/C_{sat}	$C(L_c(t))/C_{sat}$	$C(L_c(t))/C_{eq}$
360	0	0.13	1.0003	1.0003	1
370	0.0625	0.14	1.00091	1.001	1.0000898
380	0.125	0.15	1.00151	1.00172	1.0002096
390	0.1875	0.16	1.00212	1.00242	1.0002993
400	0.25	0.17	1.00274	1.00312	1.0003888
410	0.3125	0.17	1.00335	1.00374	1.0003888
420	0.375	0.17	1.00396	1.00435	1.0003888
430	0.4375	0.17	1.00457	1.00496	1.0003888
440	0.5	0.17	1.00518	1.00557	1.0003888

and taking into account the variation of P_{cap} with t, one obtains an estimate of $P_c(L_c(t))$ as a function of time. Using eqn (1), the ion mass fraction ratio $C(L_c(t))/C_{sat}$ corresponding to $P_c(L_c(t))$ can be determined (Table 1). Finally, one can also determine the ratio $C(L_c(t))/C_{eq}$ (Table 1). As can be seen from Table 1, $C(L_c(t))/C_{eq}$ varies in the range [1–1.0004]. The upper bound of this range ($\sim$1.0004) is greater but close to the ion mass fraction computed from the film model (Fig. 6) indicating that $C(L_c(t))/C_{eq} \sim 1.00013$ at the entrance of the film where ions in excess are necessary for generating the extra stress and the transverse growth of the crystal front face. Based on the approximations made to obtain the various estimates, we conclude that the estimate of the supersaturation at the entrance of the film obtained from the mechanical considerations is consistent with the supersaturation obtained from the film model. Nevertheless, more refined analyses, probably implying detailed numerical simulations (for instance in the spirit of the work presented in ref. 25), are desirable to reach still more firm conclusions.

3.7 Collapse mechanism

Then we are left with the explanation for the collapse itself. Since the liquid is not replaced by gas in the collapsing region, the crystal region acts as a barrier preventing the gas from reaching the liquid region located between the crystal and the channel dead-end. Also, we note that no bubble formation is observed in the collapsing region. Based on the elastic modulus E of PDMS (E = 1.2 MPa, see the ESI of ref. 11), and assuming purely elastic deformation, the numerical computation on the collapse presented in ESI† Appendix G indicates that a negative pressure on the order of -5 bars (-0.5 MPa) is sufficient to cause the observed collapse. Consistently with the observation, this is much less than the negative pressure required for the formation of a bubble by cavitation (~ -9 MPa according to ref. 26).

As sketched in Fig. 5 and 6, we assume that a liquid film is confined between the crystal and the walls all along the crystal with a meniscus present at the film tip on the side of the crystal back face when the liquid plug on the left of the crystal in Fig. 1 disappears. It is surmised that the curvature of this meniscus adjusts in response to the pressure decrease of the solution induced in the collapsing region by the pervaporation. For $p_s - P_{atm} \sim -5$ bars, *i.e.* on the order of magnitude of the negative pressure in the solution to observe the collapse, applying Laplace's law, *i.e.* $p_s = p_{atm} - \gamma/r$, gives $r \approx 170$ nm (with a contact angle $\sim 90^\circ$ on the PDMS wall and a zero contact angle on the crystal,[27] r is the curvature radius depicted in Fig. 5, γ is the surface tension, and $\gamma \approx 83 \times 10^{-3}$ N m^{-1} for a saturated NaCl aqueous solution). The meniscus curvature in the film plane is neglected since the film thickness is much smaller that the channel width. This curvature radius is greater than the expected thin film thickness h.[22] For this reason, within the framework of the liquid film assumption, the liquid–gas interface must remain stuck at the tip of the liquid film on the back of the crystal during the collapse.

Then, a simple idea is to consider that the liquid mass loss by pervaporation in the collapsing region induces the increase in the curvature of the liquid–gas interface. As a result, the pressure in the solution decreases, *i.e.* is more and more negative. Thus, the collapse would result from the combination of pervaporation and capillary effects. However, it has been shown, *e.g.* ref. 18, that significant negative pressures can also be induced by the pervaporation process in a liquid pocket surrounded by PDMS. In our experiments, this would correspond to the situation where the crystal is in direct contact with the PDMS walls so as to hydraulically isolate the collapsing liquid plug. In other terms, this situation is only possible if one considers that the liquid film between the crystal and the PDMS disappears. For instance, one might consider that the air–liquid interface moves between the PDMS and the crystal. However, this would mean curvature radii of the order of the film thickness and thus capillary pressures not consistent, *i.e.* much too big, with the pressure levels corresponding to the collapse. Also, as discussed in Section 3.5, the presence of the liquid film is necessary to explain the increase in the channel width in the crystal region before the collapse occurs and to explain that the crystal continues to grow transversally during the collapse, on the side of the collapsing plug. However, again, we have no direct proof of the existence of the meniscus. Simply, we obtain results consistent with the observations with the assumption of the presence of a meniscus at the tip of the film on the crystal back face side. As already mentioned in Section 3.5, the film is perhaps only present where the transversal crystal growth occurs, *i.e.* on the crystal front face side, with no meniscus. In this case, capillary effects cannot be invoked to create the negative pressure leading to collapse. In this case, the pervaporation would be responsible for the negative pressure generation. In this respect, as suggested by a reviewer of the original version of the paper, an interesting experiment could be to collapse the entrance of the channel (loaded with NaCl solution or pure water) by applying a pressure and observe whether or not pervaporation does lead to pore collapse in the dead-end section. Nevertheless, it can be observed that the crystal is bounded by a glass wall and not by PDMS on one lateral side. There is no pervaporation through the glass and the presence of a liquid film between the glass wall and the crystal is therefore still more plausible. Thus, the capillary pressure needed for generating the negative pressure could be due to a meniscus present between the crystal and the glass wall at the tip of the film (if again we consider that the meniscus is stuck on the crystal front face side because the

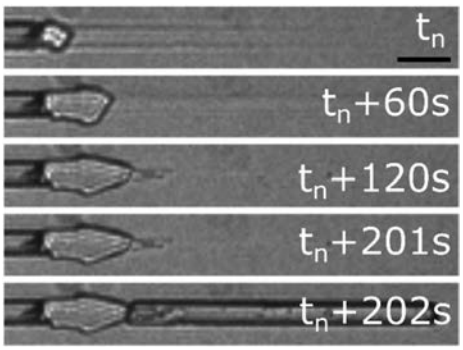

Fig. 7 Example of channel collapse and instantaneous re-opening at the end of pervaporation. The re-opening occurs a few seconds after the end of the collapse. Black scale bar is 10 μm.

capillary pressure needed for the collapse is too low for the meniscus to recede between the wall and the crystal).

3.8 After the collapse

Also an additional interesting phenomenon can be observed after the collapse but not always. As illustrated in Fig. 7, it can happen that the channel reopens after the collapse. In the example shown in Fig. 7, the reopening occurs about 80 s after the end of collapse. This is consistent with the disappearance of the thin film due to pervaporation. The mass of solution in the film is $m_{\text{film}} = \rho_\ell L_c h W$ (considering only one lateral face of the crystal). The pervaporation rate is $J_{\text{pe}} = \rho_\ell v_{\text{pe}} W L_c$. Thus, a characteristic time for the disappearance of the film by pervaporation is $t = m_{\text{film}}/J_{\text{pe}} = h/v_{\text{pe}}$. With $v_{\text{pe}} \approx O(10^{-8}\ \text{m s}^{-1})$ (see ESI† Appendix E), this gives $t \approx$ 1–10 s for $h \sim$ 10–100 nm. This estimate of the film disappearance time is compatible with the observation. The greater value observed in the experiment might be due to the presence of small cavities at the surface of the crystals containing some extra liquid. Thus, in this case, the reinvasion of the film region by the gas phase together with the end of the capillary effect due to the liquid disappearance would lead to the channel reopening. It also happens that this channel reopening phenomenon does not occur. In this case, the channel remains collapsed and is still so after several weeks. It is surmised that the salt can sometimes fully clog the film regions forming a barrier between the gas phase in the channel on the left of the crystal in Fig. 7 and the collapsed region (contrary to water, the ions cannot leave the film region). In other words, during the pervaporation of the film, the salt precipitation can sometimes clog the film region and sometimes forms a thin zone through which the gas can percolate. Some variabilities in the adhesion forces between the PDMS walls in contact or between PDMS and glass might also play a role in these observations.

4 Conclusions

In summary, our experiments in model pores first confirm from direct optical observations that the growth of a crystal in a pore can generate a normal compressive stress on the pore wall, see ref. 11 for more details. More unexpectedly, we have shown that a normal tensile stress can be also generated. In the case of our experiments, this led to the collapse of the region located between the crystal and the model pore dead-end. It can be noted that the process actually leads to shear stress generation since a normal compressive stress and a normal tensile stress are generated together in about the same region of the pore wall. The assumption of the presence of a thin liquid film between the crystal and the wall with a meniscus at the entrance of the film leads to consistent results with the experimental observations. Within the framework of this assumption, the normal tensile stress is attributed to the negative pressure in the solution induced by a capillary effect whereas the mechanism of water loss inducing the capillary effect is attributed to the pervaporation of water through the PDMS wall of the model pores. However, owing to the pervaporation, this assumption can be questioned and we cannot exclude that perhaps the crystal completely plugs the channel (with no meniscus confined between the crystal and the pore walls). In this case, the collapse would be due to the pervaporation process only and not to a capillary effect. In any case, it can be noted that the classical expression of the crystallization pressure leads to estimated values consistent with our experiments. In other words, we have no particular reason to question the validity of eqn (1) from our results.

Again, owing to the significance of the pervaporation process in our experiments, it is not obvious to readily conclude that similar capillary effects can be generated by evaporation at the film tip in the more classical situation where the solid matrix of the porous material is impervious. This remains to be confirmed. For instance, one might use a similar approach to the one presented in the present paper but for a system where the pervaporation does not take place. In this respect, it can be noted that deformation of a porous material due to the drying of capillary bridges is reported in ref. 28. Although the situation in ref. 28 is different from the one studied in the present paper, this is an indication that deformation at the pore scale due to capillary effects is possible with an impervious solid matrix. However, it should be clear that the level of negative pressure observed in our experiments is sufficient to cause pore collapse in a soft material such as PDMS but not in a porous stone for instance. Finally, our experiments have also led us to identify and analyze a new phenomenon, the hyperslow drying process of PDMS channels.

Author contributions

A. N., P. J., and M. P. designed the research; A. N., P. J., and M. P. performed the research. All authors contributed with discussions, analysis and interpretation of experimental data and modelling results. M. P. wrote the manuscript and all authors edited it.

Conflicts of interest

There are no conflicts to declare.

Notes and references

1 L. N. Nassar and T. Horton, *Soil Sci. Soc. Am. J.*, 1999, **63**, 752.
2 X. Y. Chen, *Aust. J. Soil Res.*, 1992, **30**, 429.
3 H. Eloukabi, N. Sghaier, S. Ben Nasrallah and M. Prat, *Int. J. Heat Mass Transfer*, 2013, **56**, 80.
4 A. Goudie and H. Viles, *Salt Weathering Hazards*, Wiley, Chichester, 1997.
5 G. W. Scherer, *Cem. Concr. Res.*, 2004, **34**, 1613.
6 R. J. Flatt, F. Caruso, A. M. A. Sanchez and G. W. Scherer, *Nat. Commun.*, 2014, **5**, 4823.
7 M. Schiro, E. Ruiz-Agudo and C. Rodriguez-Navarro, *Phys. Rev. Lett.*, 2012, **109**, 265503.
8 C. Rodriguez-Navarro and E. C. Doehne, *Earth Surf. Processes Landforms*, 1999, **24**, 191.
9 M. Steiger, *J. Cryst. Growth*, 2005, **282**, 455.
10 J. Desarnaud, D. Bonn and N. Shahidzadeh, *Sci. Rep.*, 2016, **6**, 30856.
11 A. Naillon, P. Joseph and M. Prat, *Phys. Rev. Lett.*, 2018, **120**, 034502.
12 J. Desarnaud, H. Derluyn, J. Carmeliet, D. Bonn and N. Shahidzadeh, *J. Phys. Chem. Lett.*, 2014, **5**, 890.
13 A. Naillon, P. Duru, M. Marcoux and M. Prat, *J. Cryst. Growth*, 2015, **422**, 52.
14 A. Naillon, P. Joseph and M. Prat, *J. Cryst. Growth*, 2017, **463**, 2017.
15 J. Stefan, *Sitzungsber Math-Naturwiss. Akad. Wiss. Wien*, 1871, **63**, 63.
16 G. C. Randall and P. S. Doyle, *Proc. Natl. Acad. Sci. U. S. A.*, 2005, **102**, 10813.
17 J. Leng, B. Lonetti, P. Tabeling, M. Joanicot and A. Ajdari, *Phys. Rev. Lett.*, 2006, **96**, 084503.
18 M. P. Milner, L. Jin and S. B. Hutchens, *Soft Matter*, 2017, **13**, 6894.
19 A. Merlin, J. B. Salmon and J. Leng, *Soft Matter*, 2012, **8**, 3526.
20 S. J. Harley, E. A. Glascoe and R. S. Maxwell, *J. Phys. Chem. B*, 2012, **116**, 14183.
21 G. W. Scherer, *Proc. 9th Int. Cong. Deterioration and Conservation of Stones*, 2000, 187.
22 F. Kohler, L. Gagliardi, O. Pierre-Louis and D. K. Dysthe, *Phys. Rev. Lett.*, 2018, **121**, 096101.
23 J. W. Mullin, *Crystallization*, Butterworth Heinemann, Oxford, 4th edn, 2001.
24 J. N. Israelachvili, *Intermolecular and surface forces*, Academic Press, Amsterdam, 3rd edn, 2011.
25 L. Gagliardi and O. Pierre-Louis, *New J. Phys.*, 2018, **20**, 073050.
26 X. Noblin, N. O. Rojas, J. Westbrook, C. Llorens, M. Argentina and J. Dumais, *Science*, 2012, **335**, 1322.
27 T. Corti and U. K. Krieger, *Appl. Opt.*, 2007, **46**, 5835.
28 M. Bouzid, L. Mercury, A. Lassin, J. M. Matray and M. Azaroual, *J. Colloid Interface Sci.*, 2011, **355**, 494.